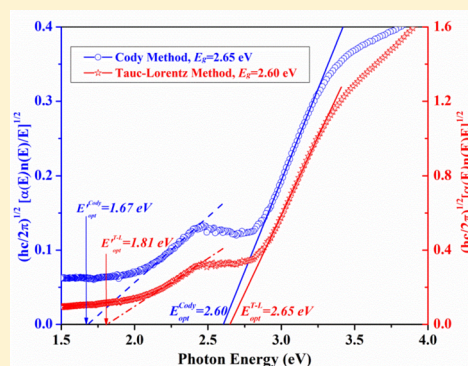


Determination of the Insulation Gap of Uranium Oxides by Spectroscopic Ellipsometry and Density Functional Theory

Heming He,[†] David A. Andersson,[‡] David D. Allred,[§] and Kirk D. Rector^{*,†}[†]Chemistry Division and [‡]Material Science and Technology Division, Los Alamos National Laboratory, Los Alamos, New Mexico 87545, United States[§]Department of Physics and Astronomy, Brigham Young University, Provo, Utah 84602, United States

ABSTRACT: Detecting and understanding the complex signatures of species for attribution of highly enriched uranium, HEU, is challenging even though these compounds have been intensively studied for 65 years. Attempts to obtain, for example, chemical speciation signatures on uranium oxides are frustrated by the presence of extremely diverse phases, complex structures, and their tendency to form solid solutions with the coexistence of many nonstoichiometric oxides. More importantly, the spectroscopic signatures of many of these oxides, using common techniques such as X-ray diffraction or Raman scattering, are remarkably similar with each other. On the other hand, the effort to understand the U–O system also exhibits some of the most intriguing and challenging properties in theoretical and computational chemistry. This is due to the spatial extent between localization and delocalization of the 5f orbitals of the uranium atom. In this article, spectroscopic ellipsometry (SE) measurements and a comparison of six fitting methods as well as theoretical calculations are combined to examine the intrinsic electronic structure and the corresponding band gap of uranium oxides to determine the chemical speciation in a ~102 nm thick reactively sputtered uranium oxide film. The SE results reveal that the UO_x film exhibits two absorption edges, a primary absorption edge slightly above 2.6 eV and a secondary absorption at 1.7–1.8 eV. The optical band gaps compared with the theoretical calculations performed on UO_2 , U_4O_9 , U_3O_7 , $\alpha\text{-U}_3\text{O}_8$, $\alpha\text{-UO}_3$, $\delta\text{-UO}_3$, and $\gamma\text{-UO}_3$ suggest that the UO_x film is composed of at least two components; the primary absorption is caused by the $\alpha\text{-UO}_3$ sublayer, which is superimposed on top of an adjacent $\alpha\text{-U}_3\text{O}_8$ sublayer that is hypothesized to be heteroepitaxial growth of $\alpha\text{-U}_3\text{O}_8$ along the UO_x /substrate interface. Comparison to the ellipsometry measurements shows that the DFT+U and hybrid (HSE) calculations predict the correct trend for band gaps as a function of oxidation state and crystallography but they fail to capture the exact gaps. However, they provide important information for interpretation of the experimental results and highlight some of the structural complexity that prevails in the UO_x compounds. The combination of theoretical and experimental methods to examine the intrinsic electronic structure and the band gap of the corresponding uranium oxides could benefit from the development of new methods for better distinguishing chemical speciation in uranium oxides. In addition, the experimental measurement of the indirect band gap of $\alpha\text{-U}_3\text{O}_8$, is, to our knowledge, reported for the first time.



1. INTRODUCTION

Fissile materials, such as uranium highly enriched in the isotope uranium-235 (HEU), are essential in building a nuclear device. The importance to national security of being able to detect these materials grows as the potential for theft and diversion of nuclear materials increases. Uranium oxidation occurs inevitably following exposure to air and masks incredibly complex speciation of oxides. The compositions and structures of these oxides are numerically variable and could carry information about environmental conditions. Therefore, the emphasis here is to characterize the speciation signatures of the uranium oxides that could provide information related to the provenance, age, and fate of the material.

Attempts to obtain, for example, chemical speciation signatures on these uranium oxides have often been frustrated by the presence of extremely diverse phases, complex structures, and their tendency to form solid solutions with

the coexistence of many nonstoichiometric oxides.^{1–3} Uranium oxides are generally intensely colored, and they can be susceptible to chemical transformations when exposed to localized heating or radiation, for example, the laser in Raman analysis. More importantly, with regard to these coexisting uranium oxides, they often lack distinguishable spectroscopic characteristics; for instance, from UO_2 to $\text{UO}_{2.25}$ (U_4O_9), the X-ray diffraction (XRD) patterns and Raman spectra are almost identical, with only a slight shift in the peak positions or intensities.² This degeneracy problem increases for nanometer scaled materials, which can suffer from additional band broadening effects. Similarly, this degeneracy is also true for $\alpha\text{-U}_3\text{O}_8$ and $\alpha\text{-UO}_3$.

Received: January 31, 2013

Revised: June 6, 2013

Published: June 7, 2013

Behind the incredible complexity of the uranium–oxygen system and its unusual structural chemistry remain many mysteries to be uncovered.^{4,5} On the other hand, the complexity of the U–O system could potentially provide almost limitless persistent characteristic signatures related to the origin and age of materials long after release. Here, multiangle, spectroscopic ellipsometry (SE) is used to report the optical properties of a reactively sputtered, 102 nm thick uranium oxide thin film from 1.25 to 6 eV. This noncontact, nondestructive technique is a versatile and powerful methodology for determination of dielectric properties of thin films on either transparent or opaque substrates.^{6,7} The technique can also yield information about layers that are thinner than the wavelength of the probing light itself, even down to a single atomic layer.⁸ From the data, the dielectric function, which gives access to intrinsic sample properties, is determined. Further, from this, the optical band gaps are determined by fitting the experimental data to appropriate models.^{9,10} The SE measurement also allows for quantitative measurement of the sublayer thicknesses of multilayer oxide thin films.⁹

The U–O system also exhibits some of the most intriguing and challenging properties in theoretical and computational chemistry. The challenge arises from the spatial extent of the 5f orbitals and the competition between localization and delocalization of these uranium orbitals. Standard density functional theory (DFT) applying the LDA or GGA exchange–correlation functionals to UO_x encounters difficulties due to the strongly correlated nature of the U 5f electrons. For example, using these formalisms, UO_2 is inaccurately predicted to be a metal.¹⁰ Inaccurate description of the band gaps of semiconductors and insulators is a well-known deficiency of DFT.¹⁰ Obviously, direct applying this methodology is not appropriate for studying band gaps in UO_x compounds. There are a number of different ways to improve the predictions of standard DFT for UO_x , especially with respect to band gap properties, including the DFT+*U* methodology,¹¹ hybrid functionals,^{12,13} and the self-interaction corrected local spin density approximation.¹⁴ Of these, DFT+*U* is the computationally most efficient technique, and it has been applied extensively to similar problems.^{15–17} Most existing studies have focused on properties of fluorite-derived UO_{2+x} compounds, and higher oxides have only received limited application of the DFT+*U* methodology. One reason for this is the uncertainty regarding the correct value of the intraband spherically averaged screened Coulomb energy (*U*) in this composition space. The present work does not address this issue per se but instead extends the approach already applied to UO_2 compounds to higher oxides, similar to the work of Yun et al.¹⁸ Hybrid functionals^{12,19} are better suited to address this problem, and they are also used in this study; however, due to the higher computational cost, some of the nonstoichiometric UO_{2+x} phases and higher oxides could not be modeled with this approach. Comparison to the ellipsometry measurements shows that the DFT+*U* and hybrid calculations predict the correct trend for band gaps as a function of oxidation state and crystallography but they fail to capture the exact gaps. However, even at this level, they provide important information for interpretation of the experimental results and highlight some of the structural complexity that prevails in the UO_x compounds.

In this article, SE measurements and DFT calculations are combined to examine the intrinsic electronic structure and the correlated band gap of uranium oxides for determination of the chemical speciation in a nanometer thin uranium oxide film.

The SE result shows the presence of two absorption features, a primary absorption edge slightly above 2.6 eV and a less intense absorption feature at 1.7–1.8 eV. Theoretical calculations performed on UO_2 , U_4O_9 , U_3O_7 , $\alpha\text{-U}_3\text{O}_8$, $\alpha\text{-UO}_3$, $\delta\text{-UO}_3$, and $\gamma\text{-UO}_3$ suggest that this UO_x film is composed of at least two components. The primary absorption is caused by an $\alpha\text{-UO}_3$ sublayer, which is superimposed on top of an adjacent $\alpha\text{-U}_3\text{O}_8$ sublayer that is hypothesized to be heteroepitaxial growth of $\alpha\text{-U}_3\text{O}_8$ along the UO_x /substrate interface. It is demonstrated that the combination of theoretical and nondestructive experimental efforts to examine the intrinsic electronic structure and the corresponding band gaps of the uranium oxides could aid in determining or distinguishing chemical speciation in other systems. In addition, the experimentally measured band gap of $\alpha\text{-U}_3\text{O}_8$, as well as its indirect absorption feature, is reported, to our knowledge, for the first time.

2. EXPERIMENTAL AND COMPUTATIONAL METHODOLOGY

2.1. Uranium Oxide Thin Film Deposition. The uranium oxide film used in our study was deposited on a 7.6 cm diameter, 1 cm thick, polished crystalline quartz substrate by reactive, DC magnetron sputtering from a depleted uranium target in oxygen/argon ambient at a pressure of ~ 0.38 Pa. The ratio of oxygen-to-total pressure (argon + oxygen) in this experiment was set to be $\sim 0.21 \pm 0.02$. For elements, like uranium, which can form many different oxides, the oxygen partial pressure is critical. Therefore, the relative argon and oxygen flow rates were carefully set and monitored. The oxygen flow was set first because oxygen was the minor gas. A Varian sapphire valve was used because it is capable of controlling very low flows of gas. The argon flow was controlled using a mass flow controller and was set second. These pressures were determined using a capacitance manometer. One advantage of a capacitance manometer is that its response is independent of the gas composition. Another advantage is that it is not affected by the plasma during deposition, whereas an ion gauge would be. During deposition, the oxygen partial pressure drops by about half, indicating that oxygen is being incorporated in the growing film.

The vacuum sputtering system was roughed with the standard rotary vane pump. When the pressure reached 100 Pa, a turbomolecular pump was started. When sufficiently low pressure (<0.1 Pa) was reached, an 8 in. gate was opened so that the high pumping speed of a cryopump (CryoTorr 8) could bring the system quickly to a base pressure of $<2 \times 10^{-4}$ Pa as determined by an ion gauge.

A 4 in. Meivac sputter gun used in the sputter system was mounted in the base plate of the chamber. The sputter targets, a 4 in. diameter uranium disk, face up. The substrate holder is mounted on an arm that can be rotated from above to pass the substrates over the sputter target one at a time.

Because thickness uniformity facilitates accurate ellipsometric characterization, efforts were made to achieve small cross-substrate thickness variation. Sputtering, particularly from a large target, as compared to evaporation, is inherently capable of producing better uniformity without the use of planetaries because the atoms emerged from a distributed, rather than a point, source. In this case, the Meivac 4 in. MAK sputter gun employed produces a circular racetrack erosion pattern on the surface of the uranium target. (It has little erosion at the center of the disk and less toward its outside edge but substantial erosion at a radius about 2/3 the distance from the center.)

However, to achieve thickness variation of less than a few percent across the substrate, additional efforts were taken. First, the substrate–target distance was increased to 10 cm. Second, a rotation arm was installed, and the sample tray was slowly rotated completely over the target multiple times at a constant rate during a single deposition to deposit a smooth film. However, without planetary rotation as the substrate and substrate holder revolve over the target, there will be a thickness gradient in the thin film from one side of the substrate to the other. Third, a four-step sequential reactive deposition was utilized to deposit one-quarter of the film thickness at a time, and then, the substrate holder was rotated 90° on its mounting point, the sample/substrate holder was returned to the vacuum system, and the deposition cycle was repeated. After four depositions, all four compass points were covered. This effort, coupled with rotating the sample holder slowly over the target multiple times at a constant rate during each deposition, minimized the preferential film growth and deposited a relatively smooth film with the desired uniformity and thicknesses.

2.2. Ellipsometry Methodology. A variable-angle spectroscopic ellipsometer (WVASE from J.A. Woollam Co., Inc.) with a xenon light source was employed to acquire the optical data on the thin films. Ellipsometry spectra recorded the parameters Ψ and Δ , which represent the ratio of the amplitude and phase shift (difference) for s- and p-polarization light after they reflected off of the surface of the film. These values were collected at 60, 63, 66, 69, 72, and 75° angles of incidence in a 1–6 eV photon energy range with an interval of ~ 18 meV. The experimental data were fit to different models, for example, the Tauc–Lorentz model, which is particularly suited for the analysis of amorphous semiconductors,²⁰ including an optical transition.

2.3. Computational Methodology. The DFT calculations were carried out on a total of five compositions (seven phases) using the Vienna ab initio simulation package (VASP),^{21–23} applying the projector augmented wave (PAW) method.^{25,26} A key challenge in modeling uranium-containing compounds is describing the 5f electrons, which are strongly correlated. In order to improve the description of U 5f electrons, the LDA+U methodology with the Lichtenstein formulation was first applied.¹¹ In the Lichtenstein formulation of the LDA+U method, the spherically averaged screened Coulomb energy, U , and the exchange energy, J , must be specified. On the basis of experimental measurements, Dudarev determined the U and J parameters to be 4.5 and 0.5 eV, respectively, for UO_2 .²⁴ In this study, $U = 4.5$ eV and $J = 0.5$ were used for all uranium oxides. However, because the U and J values may depend on atomic coordination, the assumption that the values derived for UO_2 are also valid for U_3O_8 and UO_3 is an approximation. As an aid to consider how they might differ, the Fe–O system could provide some guidance. The U values for the FeO (NaCl structure type) and Fe_2O_3 (corundum crystal structure) compounds were calculated to differ by 0.6 eV.²⁵ The facts that, first, the U_3O_8 structure is closely related to the UO_2 fluorite structure²⁶ and, second, the U^{6+} ions in UO_3 nominally have empty f orbitals (there are no 5f electrons to be considered) support the application of fluorite U and J parameters as a reasonable approach until parameters are determined for U_3O_8 and UO_3 . In addition, the screened hybrid functional developed by Heyd, Scuseria, and Ernzerhof¹⁹ was used for the compounds with small enough units cells (all but $\gamma\text{-UO}_3$, the nonstoichiometric UO_{2+x} compounds, and $\alpha\text{-U}_3\text{O}_8$)

to make them tractable by this computationally more expensive technique. The HSE06¹² version of the hybrids functionals was used here. This methodology has been shown to provide good band structure predictions,^{12,13,17,27–29} and moreover, it does not require specification of any U parameter and thus circumvents the issue of unknown changes to the U parameter as a function of the oxygen content.

The localized spins on uranium ions in UO_2 , UO_{2+x} , and U_3O_8 were assumed to order antiferromagnetically, which was also obtained as the lowest-energy configuration in the DFT calculations. For U_3O_8 , the same ordering model as that in ref 27 was applied (the spin moments are parallel within each close-packed plane and antiparallel between the planes). Other possibilities were also investigated, though these were slightly higher in energy and predicted band gaps that were a couple of tenths of an eV lower. For UO_2 and UO_{2+x} , the 1 k ordering of the magnetic moments was assumed.^{13,30,31} There are no localized moments for the UO_3 compounds due to the U^{6+} character of all uranium ions. Spin–orbit coupling and noncollinear magnetic ordering were ignored in order to simplify the calculations. The volume was relaxed for all crystal structures, and the internal structural parameters were relaxed until the Hellmann–Feynman forces on each ion were sufficiently small (0.02 eV/Å) or until the total energy was converged to at least 0.0001 eV/atom. The plane-wave cutoff was set to 500 eV. As a standard choice, Monkhorst–Pack k point meshes were used for all compounds,³² but for completeness, Γ centered grids were also used whenever possible. Even though the total energies are insensitive to this setting, the band gap is sometimes slightly reduced for the Γ centered grids. The grid densities were $8 \times 8 \times 8$ for the fluorite unit cell of UO_2 or equivalently $4 \times 4 \times 4$ for the $2 \times 2 \times 2$ fluorite supercell, $4 \times 4 \times 6$ for U_4O_9 ,³¹ $3 \times 3 \times 3$ for U_3O_7 ,³¹ $6 \times 4 \times 6$ for $\alpha\text{-U}_3\text{O}_8$ ($6 \times 4 \times 4$ for the Γ centered grid) without any symmetry restrictions and $8 \times 4 \times 8$ for $\alpha\text{-U}_3\text{O}_8$ with symmetries restricted to the experimental crystal structure, $8 \times 4 \times 8$ for $\alpha\text{-UO}_3$, $4 \times 4 \times 4$ for $\gamma\text{-UO}_3$, and $8 \times 8 \times 8$ for $\delta\text{-UO}_3$. The HSE calculations for $\alpha\text{-U}_3\text{O}_8$ and the UO_3 phases applied less dense k point meshes, that is, $4 \times 2 \times 4$ for $\alpha\text{-U}_3\text{O}_8$ (with symmetries restricted to the experimental crystal structure), $4 \times 2 \times 4$ for $\alpha\text{-UO}_3$, and $4 \times 4 \times 4$ for $\delta\text{-UO}_3$. In order to predict an accurate electronic density of states (DOS), the tetrahedron method was used for k space integration.³³

Dorado et al. showed that for UO_2 and UO_{2+x} the LDA/GGA+ U methodology may result in metastable solutions for the electronic structure due to differences in the detailed occupation matrices for the U 5f orbitals.^{31,32} Here, the occupation matrix control scheme developed by Dorado et al.^{31,32} as well as the U ramping method due to Meredig et al.¹⁶ were applied for the LDA+ U calculations. Unless explicitly stated, no assumptions were made about the crystal symmetries in the calculations. Only solutions for the Jahn–Teller distorted structure of UO_2 are presented for the LDA+ U calculations; the properties of current interest (equilibrium volume and band gaps) were found to be essentially identical for the Jahn–Teller and the ideal fluorite phases of UO_2 . A $2 \times 2 \times 2$ expansion of the fluorite unit cell was used to model UO_2 for the LDA+ U calculations, and the conventional unit cell was used for the HSE06 calculations. Additional details regarding the LDA+ U calculations are described elsewhere.³⁴

The two remaining compounds in this study U_4O_9 and U_3O_7 were modeled by the DFT-derived crystallographic models in refs 31 and 35. These may not be identical to the

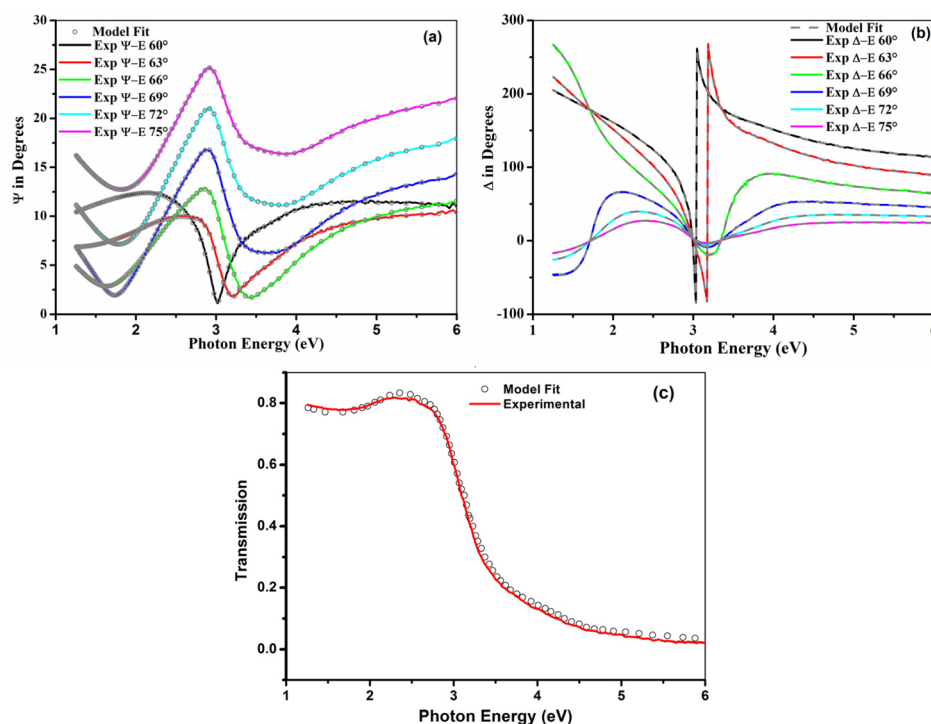


Figure 1. Ellipsometric measurement of Ψ - E (a) and Δ - E (b) as a function of photon energy for an angle of incidence from 60 to 75° with an interval of 3° and the optical transmission measurement (c). The line is the measured values. The open circles correspond to these quantities as calculated from the optical constants as determined in this study.

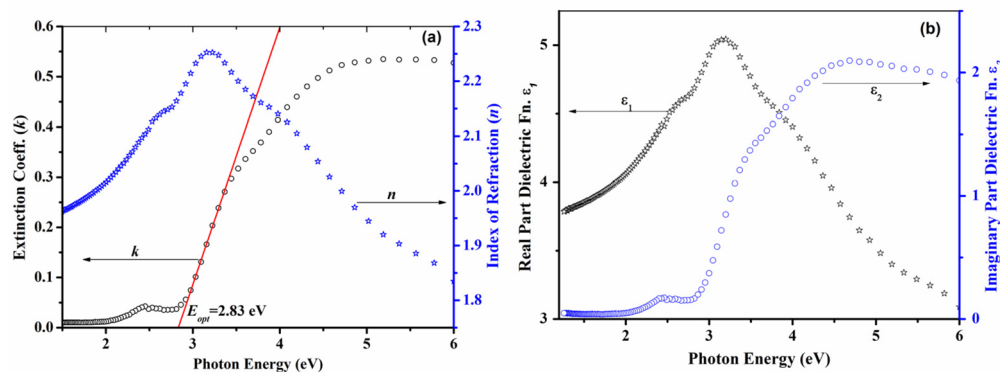


Figure 2. Optical constant of the UO_x thin film versus photon energy: (a) spectral dependence of extinction coefficients (k) and refractive indices (n); (b) real (ϵ_1) and imaginary (ϵ_2) parts of the dielectric constant. The straight line in (a) gives a calculation of the optical gap based on k (see text) for the dominant uranium oxide phase in the film.

experimentally observed phases, but they represent the lowest-energy configurations found in DFT, and from the perspective of understanding band gap properties, they should accurately represent the shift of these properties as a function of the oxygen content. The $\alpha\text{-U}_3\text{O}_8$ ³² and UO_3 (α ,³⁶ γ ,³⁷ and δ ³⁸) crystal structures were taken from the ICSD crystallographic database.³⁹ These crystallographic models used as initial structures were fully relaxed in the calculations, which resulted in slight symmetry reduction of the $\alpha\text{-U}_3\text{O}_8$, $\alpha\text{-UO}_3$, and $\gamma\text{-UO}_3$ lattices compared to the experimental references. This effect is particularly accentuated for U_3O_8 , where it is related to specific ordering of U^{5+} and U^{6+} ions.³¹ Note that this lattice relaxation impacts the predicted band gaps. In order to better represent the experimental $\alpha\text{-U}_3\text{O}_8$ phase, calculations were also performed with the experimental crystal symmetry ($C2mm$)

enforced. Except for the latter case, data for the lowest-energy solution are reported.

3. EXPERIMENTAL RESULTS

The plots of measured values of Ψ and Δ with different incidence angles as a function of photon energy are presented in Figure 1. The ellipsometry spectra show large oscillations in the Δ value, Figure 1b, which aids in fixing the films optical thickness (refractive index times thickness). The corresponding simulated ellipsometric angle curves, which are calculated according to the best-fit model parameters, are also shown in the same plots. As seen in Figure 1a, Ψ - E plot, and Figure 1b, Δ - E plot, accurate descriptions of the data are achieved for the whole range of the incidence angles. Transmission data is particularly sensitive to absorption (related to the imaginary part of the refractive index). The fact that good agreement is

obtained for the measured optical transmission data (the continuous curve in Figure 1c) using the optical constants from ellipsometry (the open cycles in Figure 1c) gives evidence that the optical constants and the thickness of the uranium oxide film have been determined well. That thickness is ~ 102 nm.

Multiangle SE is well suited to extracting the complex refractive index, N , of the film (see Figure 2a) from the measured Ψ – E and Δ – E curves once an optical model has been constructed. N , which includes a real part of the complex refractive index known as the refractive index (n) and the imaginary part of the complex refractive index also known as the extinction coefficient (k), is given by $N(E) = n(E) + ik(E)$.

There are several noteworthy features in the plot of k versus photon energy (Figure 2a). Starting at the left, there is, first, a modest absorption feature beginning at about 2.0 eV, reaching a maximum of 0.05 at about 2.4 eV. The second feature is much more intense and begins near 2.8 eV and rises rapidly. The slope changes at about 3.5 eV but continues to rise to about 4.5 eV, at which point the value of k levels off. The following discussion focuses first on the larger absorption edge, which begins at about 2.8 eV, and then on the smaller absorption feature at around 2.4 eV.

Figure 2b shows the real (ϵ_1) and imaginary (ϵ_2) parts of the dielectric functions versus the photon energy (eV) obtained from ellipsometric measurements using the following procedures. n and k of the UO_x /quartz sample were determined by fitting the experimental Ψ and Δ spectra, Figure 2a. The dielectric functions ϵ_1 and ϵ_2 were calculated from the complex index of refraction n and k by eqs 1a and 1b

$$\epsilon_1(E) = n(E)^2 - k(E)^2 \quad (1a)$$

$$\epsilon_2(E) = 2n(E)k(E) \quad (1b)$$

and displayed in (Figure 2b). Below the band gap, the imaginary component of the complex refractive index k is close to 0; therefore, the above equations approximate to $\epsilon_1 \approx n^2$ and $\epsilon_2 \approx 0$ in this region. Both the ellipsometric and transmission optical data are well fit with these constants. This provides confidence in the derived values of the optical constants and film thickness.

4. RESULTS AND DISCUSSION

4.1. Determination of Optical band gaps Using Spectroscopic Ellipsometry. Six methods for determining the band gap from the optical constants displayed in Figure 2 are presented, following the approach as described in the literature,⁴⁰ where the first three are based on linear extrapolation of simple optical parameters and the other three are based on dispersion models. Briefly, and in more detail below, in the first method, the absorption edge of the extinction coefficient k curve is linearly fit to extract the energy for the onset of absorption that is taken to be the optical band gap, as shown in Figure 2a; the second and third methods that have been used to extract the optical band gap employ the imaginary part of the dielectric function (ϵ_2) and the absorption coefficient (α), Figure 3. Moreover, the Tauc method (the fourth) will be utilized to determine the direct or indirect band gap of the film by extrapolation of a straight line to $(ah\nu)^{1/m} = 0$, in the $(ah\nu)^{1/m}$ versus photon energy plot.⁴¹ Finally, the fifth and sixth methods involve more precise reporting of the optical band gap value from two different expressions for the imaginary part of the dielectric constant, Tauc–Lorentz (T–L) and Cody models.

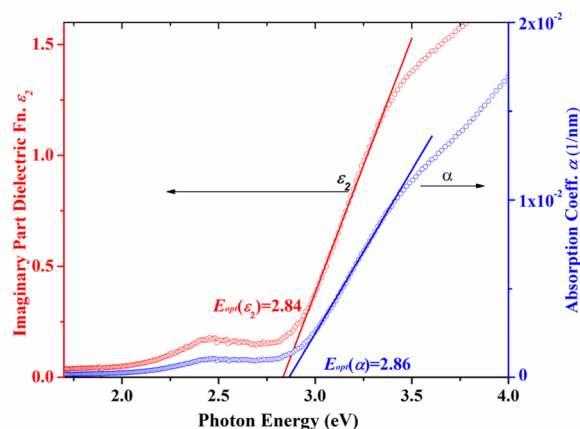


Figure 3. Band gap of the ~ 102 nm UO_x film obtained by linear extrapolation of the dielectric function ϵ_2 and the absorption coefficient α .

In the first three methods to determine optical band gaps, Figures 2a and 3 show the optical band gaps determined by linear extrapolation of the extinction coefficient k curve (Figure 2a), the dielectric function (ϵ_2), and the absorption coefficient α (Figure 3) on the ~ 102 nm UO_x thin film. The linear fits were conducted on the lower portion of the curves but excluded the lowest-energy portion, where the Urbach tail might lie.⁴² Using this methodology, the optical band gap was determined to be $E(k) = 2.83$ eV, $E(\epsilon_2) = 2.84$ eV, and $E(\alpha) = 2.86$ eV. The imaginary part of the dielectric function (ϵ_2) and the absorption coefficient (α) are all related to the extinction coefficient (k) by simple functions; see eqs 1b and 2

$$\alpha(\nu) = \frac{4\pi k(E)E_{\text{opt}}}{hc} \quad (2)$$

Therefore, the first three methods are nearly equivalent, and the optical band gap (E_{opt}) values determined by them agree well with slightly larger E_{opt} using the α method than ϵ_2 and k methods by a value of 0.02 and 0.03, respectively. The reason for this is that an extra factor of E is gained when converting from k or ϵ_2 to α . This factor of E adds an additional concave nature to the absorption coefficient curve, which has the effect of shifting the linearly extrapolated optical band gap to higher energy.⁴⁰

4.2. Direct and Indirect Band Gaps. Basically, the band gap represents the minimum-energy difference between the top of the valence band (VB) and the bottom of the conduction band (CB) in a material. The question is, how fast does absorption rise for energies above the band gap? In a direct band gap semiconductor, the top of the VB and the bottom of the CB occur at the same value of momentum, and this optical transition does not need phonon assistance to satisfy momentum conservation. Absorption rises quickly (parabolic). However, the top of the VB need not lie directly above the bottom of the CB in momentum space. When the maximum energy of the VB occurs at a different value of momentum than does the minimum in the CB energy, this optical transition requires phonon assistance to satisfy the momentum conservation law. Such materials are called indirect band gap materials, and absorption rises more slowly above the band gap.⁶

Davis and Mott suggested that the absorption coefficient, α , of semiconductors generally follows a relationship with the

photon energy ($h\nu$), for direct and indirect optical transitions shown in eq 3⁴¹

$$\alpha(\nu) = \frac{A(h\nu - E_{\text{opt}})^m}{h\nu} \quad (3)$$

where A is an energy-independent constant and m is a constant that determines the type of the optical transitions. The application of this relationship could be used to determine the optical band gap, E_{opt} . Figure 4 plots the variation of

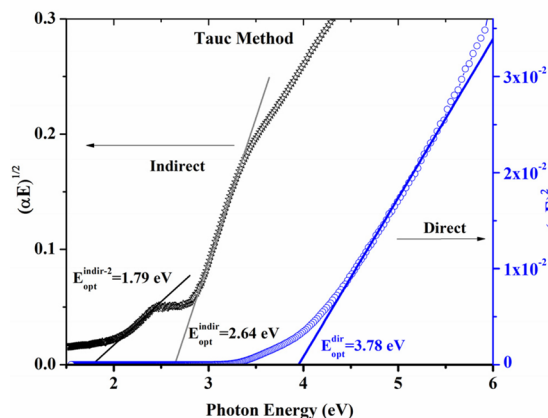


Figure 4. Tauc Plot of $(\alpha E)^{1/m}$ as a function of photon energy $E = h\nu$ for determination of the optical band gap of the ~ 102 nm UO_x thin film. The left curve ($m = 2$) suggests an indirect $E_{\text{opt}}^{\text{indir}} \approx 2.64 \pm 0.02$ eV. The curve on the right ($m = 1/2$) lacks a straight line region, suggesting that the material causing this absorption edge is not a direct band gap. A line is nevertheless drawn. The plot also allows the calculation of the gap of the weaker absorption edge as an indirect transition, located ~ 0.85 eV below the primary absorption edge. This supports the existence of two indirect band gap materials in the film, the majority/minority phases with band gaps at $2.64 \pm 0.02/1.79 \pm 0.03$ eV, respectively.

$(\alpha E)^{1/m}$ (as the ordinate) versus the photon energy, $E = h\nu$ (as the abscissa). The extrapolation of a straight line to the x axis, $(\alpha E)^2 = 0$, gives the value of the direct band gap ($m = 1/2$), while, the extrapolation of a straight line to $(\alpha E)^{1/2} = 0$ gives the value of the indirect band gap.⁴¹

Figure 4 supports the existence of two indirect band gap uranium oxide phases in the film, the majority and minority phases possessing band gaps at 2.64 ± 0.02 and 1.79 ± 0.03 eV, respectively. There are well-defined linear regions beginning near the onset of both absorption edges of the left curve described by the Tauc indirect relationship with $m = 2$.^{39,40} The curve on the right ($m = 1/2$) lacks a straight line region, suggesting that the material causing this absorption edge is not direct band gap. While a line was drawn with an intercept of about 3.78 eV, it is clear that the line is not unique. The plotted data lack a straight line region. Rather, the curve is bowed up. The plot also allows the identification of the weaker absorption edge also as an indirect allowed transition, located ~ 0.85 eV below the primary absorption edge. This indicates the existence of another indirect band gap material in the film. In short, this uranium oxide film is comprised of at least two indirect band gap materials. This conclusion may be partially supported by the visible appearance of good transparency with a light yellow color of the film compared to UO_2 , a direct band gap material, which is colored opaque and dark. Indeed, the color of a uranium oxide could depend on the oxidation state of U, the

microstructure, and the crystallite size, but more importantly, it depends on the intrinsic optical absorption properties of the oxide. It is known that light with photon energy close to the band gap can penetrate much farther before being absorbed in an indirect band gap material than a direct band gap one. Indirect band gap materials do not absorb light well and are more likely transparent. On the other hand, other thin films have been made of the direct band gap material UO_2 ,¹³ which absorbs much of the light and consequently appears dark (band gap value ≈ 2.0 eV).

4.3. T–L and Cody Dispersion Models. There are two other models providing alternate methods to extrapolate the position of the indirect optical band gaps in the two materials in the UO_x film. Both begin by using ϵ_2 rather than α alone in the square root that defines the ordinate in these plots. The Cody method simply replaces α with ϵ_2 .

More recently, Jellison and Modine developed the T–L expression²⁰ in which the imaginary part of the dielectric function, ϵ_2 , is determined by multiplying the Tauc joint DOS and the Lorentz oscillator function⁴³ in an attempt to obtain a suitable description of the near-gap and above-gap optical responses, respectively. In this model, the imaginary part of the dielectric function $\epsilon_2(E) = 2n(E)k(E)$ is taken to be proportional to $(E - E_{\text{opt}})^2/E^2$. This expression can be rearranged to give the following equation when E is near the optical band gap, E_{opt} :

$$E - E_{\text{opt}} \propto \sqrt{\epsilon_2(E)E^2} = \sqrt{\frac{hc}{2\pi}} \sqrt{\alpha(E)n(E)E} \quad (4)$$

Thus, in the T–L model, the right side of eq 4 is plotted versus the photon energy (right curve in Figure 5). While the

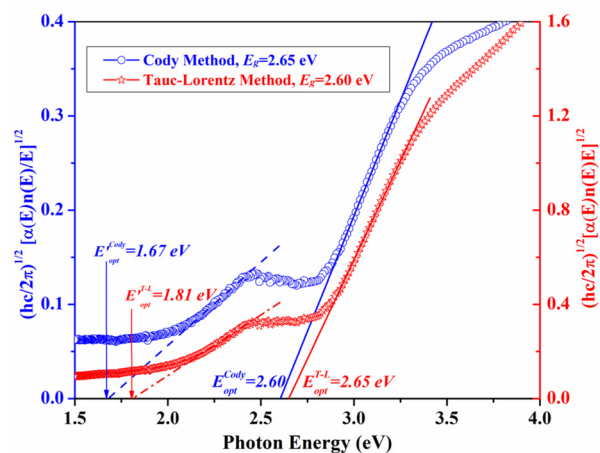


Figure 5. Comparison of T–L and Cody methods for determination of the optical band gap on the ~ 102 nm U–O thin film.

T–L expression has led to improved fits of ellipsometric spectra in some cases and currently represents the most widely used parametrization of the optical functions of amorphous semiconductors,⁴⁴ it does not improve the straight-line region for the 102 nm UO_x film. The optical gap as determined from the T–L plot is insignificantly larger (only 0.01 eV) than the value obtained using the Tauc model.

According to Tauc's relationship for the allowed indirect transition, the values of the optical band gap, E_{opt} , calculated as the intercept of $(\alpha h\nu)^{1/2}$ versus $h\nu$ at $(\alpha h\nu)^{1/2} = 0$, are expressed as the Tauc gap (2.64 ± 0.02 eV).⁴⁵ Much earlier,

Cody and co-workers published an expression⁴⁶ in which $\alpha(E)$ in the Tauc expression is replaced by ε_2 ; see eq 5. This expression can be rearranged to give eq 6

$$\varepsilon_2(E) = A_T(E - E_{\text{opt}})^2 \quad (5)$$

$$E - E_{\text{opt}} \propto \sqrt{\varepsilon_2(E)} = \sqrt{\frac{\hbar c}{2\pi}} \sqrt{\frac{\alpha(E)n(E)}{E}} \quad (6)$$

where the two constants to be fit are A_T and the optical band gap, E_{opt} . Thus, the Cody gap can be determined from the energy position $(\varepsilon_2)^{1/2} = 0$ in the plot of $(\varepsilon_2)^{1/2}$ versus $h\nu$, Figure 5. While it is claimed that the Cody model provides superior fitting to experimental spectra than the Tauc model,⁴¹ it is noted that, in this study, its linear range is smaller than that of T–L or Tauc and yields an estimation of the gap that is slightly smaller (0.04 eV) than Tauc or T–L.

The spread in the optical gaps for the smaller absorption feature that reaches a maximum of about 2.4 eV is larger than that for the large feature. The Cody, Tauc, and T–L methods give 1.67 ± 0.04 , 1.79 ± 0.03 , and 1.81 ± 0.03 eV, respectively, for this feature. At this point, it is useful to compare these results with experimentally determined band gaps. $\alpha\text{-UO}_3$ is reported to have a band gap of ~ 2.61 eV,⁴⁷ which suggests that $\alpha\text{-UO}_3$ is likely one of the phases present. Indeed, XRD measurements performed on the same uranium oxide thin film sample also suggest that the primary phase of the uranium oxide thin film is $\alpha\text{-UO}_3$.⁴⁸ $\alpha\text{-UO}_3$, which is stable under ambient conditions and generally regarded as a uranium-deficient form of $\alpha\text{-U}_3\text{O}_8$, has an unusual structure with a large concentration of disordered cation vacancies and ordered anion vacancies.⁴⁹

The band gap of the small absorption feature does not match any uranium oxide whose band gap is known. It corresponds to U_3O_8 for reasons that will become clear when the DFT calculations are discussed below.

It is clearly not due to an Urbach tail for these reasons:

(1) An Urbach tail describes absorption that declines exponentially away from a band edge.⁴² It does not rise to a maximum as is observed in this case.

(2) The position is almost 1 eV below the primary optical band gap E_{opt} (Figures 4 and 5). It is clear that the disorder in the U–O framework or crystallinity in grain boundaries would not be able to create defect states that are shifted by 1 eV. The band edge defect state E_{def} is normally located 0.2–0.3 eV below the optical band gap energy E_{opt} .^{50,51}

(3) This additional absorption edge is not seen in thin-film uranium oxide samples deposited at higher oxygen partial pressures (40–70%, data not shown) than those used to prepare this film ($\sim 20\%$). However, it is observed in low oxygen partial pressures. Higher oxygen partial pressure could be expected to eliminate uranium oxide phases containing lower oxygen content.

4.4. DFT Calculations: Results and Discussion. The calculated total DOS for UO_2 , U_4O_9 , U_3O_7 , $\alpha\text{-U}_3\text{O}_8$, $\alpha\text{-UO}_3$, $\delta\text{-UO}_3$, and $\gamma\text{-UO}_3$ are shown in Figure 6 (from LDA+U). The calculated band structure of UO_2 is direct, which is a conclusion supported by other researchers who have calculated its band structure.^{18,52} This gives confidence that DFT may help identify the phases in the UO_x film studied. The band gaps and lattice volumes derived from the calculations compared to experimental values of the respective phases are summarized in Table 1, together with results from the HSE06 calculations. The

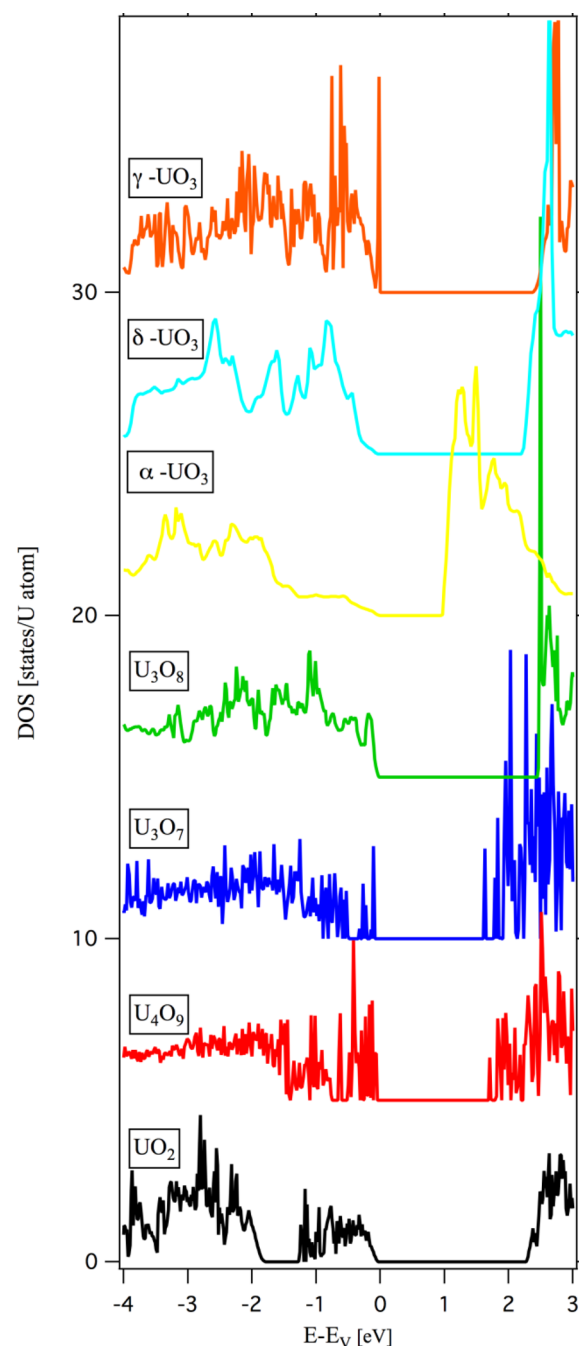


Figure 6. Calculated DOS for UO_2 , U_4O_9 , U_3O_7 , $\alpha\text{-U}_3\text{O}_8$, $\alpha\text{-UO}_3$, $\delta\text{-UO}_3$, and $\gamma\text{-UO}_3$ from the LDA+U method in the band gap region (O 2p dominated VB plus the bottom of the CB). Because the spin-up and spin-down channels are essentially identical, only the spin-up channels are shown. The energy of the highest occupied state is set to 0 eV.

calculated band structures show that $\alpha\text{-UO}_3$ and $\alpha\text{-U}_3\text{O}_8$ are indirect band gap materials, which is evidenced by the data in Table 2. This fact and the computed values of the band gaps (Table 1 and below) suggest that these may correspond to the large and small absorption features, respectively.

One complex and interesting phenomenon that dominates the chemistry and physics properties of actinide species is the spatial extent of their 5f orbitals.^{53–55} Moreover, the strong correlation between 5f electrons influences the properties of actinide compounds, in particular, for UO_2 , where the cation is

Table 1. Experimentally Determined Optical Gaps, Calculated Lattice Volumes, and Band Gaps Using DFT+*U* and Hybrid Functionals (HSE06) on Some Uranium Oxide Phases^a

	method	UO ₂	U ₄ O ₉	U ₃ O ₇	α -U ₃ O ₈	α -UO ₃	δ -UO ₃	γ -UO ₃
DFT calculated	band gap LDA+ <i>U</i> (eV)	2.27	1.68	1.59	2.43/2.06	0.94	2.19	2.35
	band gap HSE (eV)	2.71	—	—	—	3.10	3.21	—
	volume, LDA+ <i>U</i> (Å ³ /U atom)	40.37	39.94	39.78	55.48/55.4	53.91	71.21	57.72
	volume, HSE (Å ³ /U atom)	40.61	—	—	54.49/54.8	59.33	69.27	—
Experimental values	literature							
	optical gap (eV) ⁴⁷	2.0			—	2.61	2.17	2.38
	volume (Å ³ /U atom)	40.87			55.55	56.60	72.25	59.35
	this Work							
	optical gap (eV)				Cody method Tauc method T–L method	1.67 ± 0.04 1.79 ± 0.03 1.81 ± 0.03	2.60 ± 0.03 2.64 ± 0.02 2.65 ± 0.02	

^aThe two values obtained on α -U₃O₈ refer to full relaxation and a relaxation with restrained crystal symmetry, respectively. The results are also compared to available literature experimental values.

Table 2. VB and CB Maxima and Minima^a

	α -U ₃ O ₈ (lowest energy)	α -U ₃ O ₈ (symmetry restrained)	α -U ₃ O ₈ (non-ground-state magnetic ordering)	α -UO ₃ (hybrid)	α -UO ₃ (LDA+ <i>U</i>)
VB maximum [eV]	3.59/3.51	3.64/3.60	3.57/3.43	2.92/2.55	5.36/3.71
CB minimum [eV]	6.06/6.05	5.73/5.73	5.92/5.7	6.16/6.04	6.44/6.32
band gap [eV]	2.47/2.54	2.09/2.13	2.34/2.28	3.24/3.49	1.08/2.61
k point VB maximum	[0.00 0.00 0.00]	[0.00 0.00 0.00]	[0.00 0.00 0.00]	[0.00 0.00 0.00]	[0.00 0.00 0.00]
k point CB minimum	[0.50 0.50 0.00]	[0.00 0.00 0.125]	[0.50 0.00 0.00]	[0.00 0.00 0.50]	[0.50 0.50 0.50]

^aThe first VB maxima entry corresponds to the VB maxima and the second to the VB position for the CB minima. Similarly, the first CB maxima entry corresponds to the CB position for the VB maxima and the second to the CB minima. The three data sets for α -U₃O₈ correspond to the lowest-energy structure, the structure with the symmetry restrained to the experimental crystallography, and the structure with magnetic AFM ordering that deviates from the close-packed planes. For α -UO₃, results from both hybrid and LDA+*U* calculations are included. The k points are given as fractional coordinates.

formally U^{IV} with an *f*² atomic configuration. The electrons occupying the 5*f* orbital are strongly localized at the U site,⁵⁶ making the oxide an antiferromagnetic *f*–*f* Mott–Hubbard insulator with an optical gap of roughly ~2.0 eV.^{57–59} The creation of the Hubbard insulating gap is due to the predominance of strong repulsive Coulomb interaction between the two 5*f* electrons (U^{IV}, 5*f*²).⁶⁰ In the LDA+*U* calculations of Figure 6, this particular physics is modeled by the Hubbard *U* model. By using this methodology, the UO₂ band gap is calculated to be 2.27 eV in the slightly distorted fluorite phase, which is close to the value obtained for the perfect fluorite crystal structure in the most recently published literature by Dorado et al.⁶¹ This value is also close to literature values for the UO₂ band gap obtained from hybrid (HSE) calculations (2.4 eV).⁶² Our calculations give a slightly higher value of 2.71 eV, which is similar with the HSE06 result in ref 13. The origin of the slight discrepancy with the first reference⁶² is presently still unknown. In contrast, the gap is determined to be 2.0 eV experimentally.⁶³ This implies that the calculated DFT+*U* gap is ~0.3 eV higher than the experimental value.

The oxidation of UO₂ by accommodation of O interstitials into its fluorite structure, which leads to the removal of an electron from the 5*f* band, converts UO₂ to a UO_{2+x} p-type semiconductor. Hence, the band gap decreases from UO₂ to the slightly oxidized compounds UO_{2+x}, U₄O₉, and U₃O₇ due to the increasing unoccupied *f* states of U⁵⁺ ions appearing at the bottom of the CB. This decreasing trend reaches a minimum for U₃O₇ (calc. 1.59 eV) according to the DFT calculations. Subsequent oxidation and partial removal of a second electron converts UO_{2+x} to U₃O₈. The gap increases for the fully relaxed α -U₃O₈ phase to 2.43 eV, but it changes less drastically for the calculation that enforces the experimental

symmetry of the phase α -U₃O₈ (2.06 eV). The U₃O₈ band gap is quite sensitive to, for example, the magnetic ordering and lattice relaxation, which are both coupled to the lattice symmetry. As an example, if the AFM state deviates from ordering in the close-packed planes, the band gap decreases to 2.11 eV, and this compound also exhibits a stronger indirect character. Other studies have reported a gap as low as 1.2 eV and as high as 2.4 eV.²⁷ The spread was hypothesized to be related to a metastable electronic solution, and this is confirmed here by the dependence of the band gap on the assumed crystal symmetry. Finally, further oxidation leads to the removal of the remaining valence electron and all 5*f* states from the VB (except for some hybridization contributions) and follows the formation of the UO₃ insulator as well as increases the band gap to 2.19 and 2.35 eV for the δ -UO₃ and γ -UO₃ phases, respectively, according to LDA+*U*. The HSE06 calculations predict a significantly higher band gap of 3.21 eV for δ -UO₃. Generally, the electronic properties of uranium oxides are difficult to describe in electronic structure calculations. However, the LDA+*U* methodology performs satisfactorily, except in the case of α -UO₃, which has a band gap less than half (0.94 eV) of that for the other UO₃ phases. This is probably related to the structural complexity of this phase, that is, it may not be correctly represented in the present calculations. As mentioned above, the high band gap obtained for U₃O₈ may be related to ordering of the magnetic moments or lattice relaxation due to ordering of U⁵⁺ and U⁶⁺ ions. Rather good agreement is obtained for the α -U₃O₈ phase with enforced symmetry, though this configuration is higher in energy than the fully relaxed structure by 0.12 eV per formula unit. The UO₂ (2.71 eV), α -UO₃ (3.10 eV), and δ -UO₃ (3.21 eV) band gaps were also calculated using the HSE06 functional. In general, these values are higher than the LDA+*U* values, but

they capture the same relative magnitude of the band gaps. The HSE α - UO_3 band gap is closer to the experimental value than that for LDA+ U , and this is also true for the atomic volume. The DOS in Figure 6 is normalized to the highest occupied state, which, for UO_2 , is the occupied U 5f states in the gap between the O 2p dominated states and the CB. For other compounds, the highest occupied state is at the top of the O 2p band, even though for U_4O_9 , U_3O_7 and U_3O_8 , there are still f orbitals contributing to the bonding. This shift is clearly seen in Figure 6.

Now, consider the discrepancies between computational and experimental determinations of the band gap. The band gap of UO_2 given in the literature is 2.0 eV.⁴⁴ This value is significantly lower than that calculated from LDA+ U (2.27 eV) with a discrepancy of ~ 0.3 eV, Table 1. This may be because the symmetries of the crystal structures used in our DFT calculations are lower compared to those of experiments (symmetry was not enforced in the calculations).³¹ For all compounds considered, the computed lattice volume was less than the experimental. The difference is rather small, except for α - UO_3 and γ - UO_3 . The α - UO_3 phase is, however, complicated and likely includes a significant number of structural vacancies on both the metal and oxygen sublattices (about 12% but distributed between both oxygen and uranium ions to maintain the correct stoichiometry).^{49,64} This feature is not properly incorporated into the structural model in the DFT calculations. The HSE band gap improves agreement with experiments for α - UO_3 , but instead, the δ - UO_3 gap is significantly overestimated. From these results, it is not immediately clear whether the discrepancies between theory (LDA+ U) and experiments for α - UO_3 is a shortcoming of the DFT simulation method or related to the structural complexity that already identified in some experiments but not incorporated in crystallographic databases nor in these calculations. With this in mind, the α - UO_3 structure proposed in the literature⁶⁴ was investigated in a preliminary way. It was found that the volume increased when metal vacancies were introduced in the U_3O_8 structure to form UO_3 . This agrees with the fact that LDA+ U significantly underestimates the volume of α - UO_3 modeled without structural vacancies. Further investigations are needed to establish quantitative relations.

Due to the structural similarity of U_4O_9 , U_3O_7 , and possibly U_3O_8 to UO_2 , one might expect that the 0.3 eV difference between the calculated and experimental UO_2 band gap could apply to these other compounds as well. If this were to be the case, the calculated band gaps listed in Table 1 should be lowered by ~ 0.3 eV, which gives 2.00 eV for UO_2 , ~ 1.38 eV for U_4O_9 , ~ 1.24 eV for U_3O_7 , and ~ 1.76 eV for α - U_3O_8 (2.13 eV for the fully relaxed structure). On the other hand, because UO_3 formally does not contain any occupied f orbitals, its phases might be different enough from the fluorite-derived UO_{2+x} that the above correction need not be applied. The HSE06 calculations likely perform better for this case.

4.5. Origin of the Small Absorption Edge. It should be noted that the band gap values as derived from the LDA+ U or HSE06 calculations based on $E_g = E_c - E_v$, can be expected to be larger than the optical band gap by the width ΔE , where ΔE is the range of localized states in the VB or CB.⁴¹ On the other hand, the optical band gaps determined from the ellipsometry measurements made at room temperature have not taken account of the necessary correction of the E_{opt} to the value at $T = 0$ K. Even though there are slight differences in terms of the physical definition and numerical value between the DFT-

calculated value, E_g , and the value derived from the optical measurements, E_{opt} , it is still possible to get useful information by comparing the E_{opt} to the calculated E_g .

Which band gap values calculated from DFT might best match the experimental optical band gap of the small absorption edge (1.67–1.81 eV)? E_{opt} is significantly lower than the LDA+ U calculated values of UO_2 (2.27 eV) but higher than that of U_4O_9 or U_3O_7 , in particular for the corrected values. These p-type semiconductors are expected to have lower band gaps than UO_2 because both U_4O_9 and U_3O_7 can be seen as U^{5+} doped into the $\text{U}^{(IV)}\text{O}_2$ lattice creating extra holes near the CB and allowing excitation of VB electrons with a much lower band gap. Similarly, the doping of U^{5+} species into $\text{U}^{(VI)}\text{O}_3$ lattice should also lead to a decrease of the band gap compared to UO_3 phases as well. Andresen⁶⁵ from neutron diffraction and Sato⁶⁶ from electron diffraction studies of U_3O_8 have shown the presence of U^{5+} and U^{6+} in U_3O_8 and U_3O_{8-x} compositions. These observations have been further supported by later neutron diffraction studies of Loopstra.⁶⁷ Thus, the existence of only U^{5+} and U^{6+} ions in U_3O_8 is well established, whereas U^{4+} ions have not been found in U_3O_8 .⁶⁸ It is clear that the corrected LDA+ U band gap value of ~ 1.76 eV for α - U_3O_8 agrees well with the experimental value of 1.67–1.81 eV determined from SE measurements.

The α phase of UO_3 has a crystal structure similar to α - U_3O_8 , with an unusually large concentration of vacancies.⁴⁹ However, they differ one from another in their intrinsic electronic and optical properties. The similarity between the α - UO_3 and α - U_3O_8 structures^{4,69} suggests that the α - U_3O_8 could exist as a defective phase adjacent to the majority of the α - UO_3 sublayer in the film. Therefore, on the basis of the ellipsometry and DFT calculation results, this small absorption edge is caused by a defective phase of α - UO_3 , most likely due to the existence of α - U_3O_8 in the thin film. The band gap of 1.67–1.81 eV is, therefore, assigned to α - U_3O_8 as well. To the best of our knowledge, this value represents the first published band gap measurement of α - U_3O_8 and the assignment of that band gap as indirect. This assignment is also supported by other measurements. Previously, this material has been characterized using neutron reflectivity and surface-enhanced Raman spectroscopy.⁴⁸ Both surface and underlying layers of the uranium oxide materials were determined with angstrom-level resolution. The results reveal that the UO_x film is composed of three sublayers, a ~ 38 Å thick layer of α - U_3O_8 formed along the UO_x /substrate interface, the adjacent sublayer consisting of a ~ 900 Å thick single phase of α - UO_3 , and the top layer, γ - UO_3 , with a thickness of ~ 115 Å.⁴⁸ The coexistence of UO_3 and U_3O_8 could be due to the faster quenching process of vapor deposition, which normally has an effective atomic quench rate greater than 10^{12} K/s.⁷⁰ Such rapid temperature quenches could retain nonequilibrium phases via a dynamic instability that splits the front separating the stable high- and low-temperature phases.⁷¹

5. CONCLUSIONS

The optical band gaps determined by the direct linear extrapolation of the extinction coefficient k , the imaginary part of the dielectric function (ϵ_2), and the absorption coefficient (α) curves only differ by ~ 0.03 eV, with values of 2.83, 2.82, and 2.85 eV, respectively. However, when these optical band gap values are compared to the values that were obtained based on different dispersion models, a noticeable discrepancy of ~ 0.3 eV was observed. The indirect optical band gap values of 2.64 ± 0.02 , 2.65 ± 0.02 , and 2.60 ± 0.03 eV were

obtained by Tauc, T–L, and Cody models, respectively. These values are in good agreement with the known literature value of 2.61 for α - UO_3 , indicating that the chemical speciation of this thin film includes at least α - UO_3 . This agrees with experimental determination of the species published elsewhere.⁴⁸ On the basis of all of the evidence presented in the previous sections, as well as the literature value and the LDA+*U* calculation results, the dispersion models are better than the simple linear extrapolation methods in determining the optical gap of the U–O film.

Moreover, a weaker absorption, located ~ 0.85 – 0.95 eV below the α - UO_3 absorption edge, can be observed in the Tauc plot for indirect allowed transitions ($E_{\text{opt}} \approx 1.79 \pm 0.03$ eV), as well as in the Cody ($E_{\text{opt}} \approx 1.67 \pm 0.04$ eV) and T–L plots ($E_{\text{opt}} \approx 1.81 \pm 0.03$ eV), in the U–O thin film. This weaker absorption is created by the coexistence of α - U_3O_8 with the α - UO_3 in the thin film. Due to the similarity in structure, XRD analysis cannot tell the difference, but the band gap is almost 1 eV between them. Similarly, SE analysis is also applicable to distinguish between UO_2 and its numerous and complicated hyperstoichiometric derivative phases.

Another important conclusion, which can be extracted from the SE experimental results, is that the α - UO_3 and α - U_3O_8 phases are better described by the indirect Tauc relationship. The electronic band structures of α - UO_3 and the α - U_3O_8 obtained from the DFT calculation also indicate that both of them are indirect band gap materials. The indirect allowed transition of the α - UO_3 and α - U_3O_8 explain the transparency of the film, which differs significantly from the intensely colored and opaque nature of the direct allowed transition in the fluorite UO_2 film.

The experimental band gap measurements were compared to the band gaps of UO_2 , U_4O_9 , U_3O_7 , α - U_3O_8 , α - UO_3 , δ - UO_3 , and γ - UO_3 derived from LDA+*U* and, wherever possible, hybrid (HSE06) calculations. According to the calculations, the UO_2 band gap decreases by 0.6–0.7 eV for U_4O_9 and U_3O_7 , while the α - U_3O_8 band gap only decreases by 0.2 eV compared to stoichiometric UO_2 . The band gaps for δ - UO_3 and γ - UO_3 are predicted to be just below and just above that of UO_2 , respectively, by the LDA+*U* calculations, while the hybrid calculations predict a significantly higher band gap for δ - UO_3 . According to LDA+*U*, α - UO_3 has a much smaller band gap, which may be an artifact due to inaccurate crystallographic information concerning the ordering of structural vacancies in α - UO_3 .

Using the combination of experimental SE measurements and theoretical DFT calculations, the capability to determine the chemical and structural signatures on similar and complex nuclear materials, such as the uranium oxide family, is demonstrated for the first time. Thinking longer term, it is possible that the nanometer resolution of the SE measurement could establish the ability to determine the chemical speciation and depth profile of a film, which could lead to a quantitative measure of oxidation kinetics. This fundamental approach provides the ability to characterize the unique signatures of the analyte, and the rates of changes in environmental samples could enable us to assess or interpret the signatures related to the exposure duration and the environmental condition of a uranium material during fabrication and transportation. The practical implication is the ability to predict the age and fate and to assess the chemical history of uranium materials for forensic analyses.

AUTHOR INFORMATION

Corresponding Author

*E-mail: kdr@lanl.gov. Tel.: (505) 667-9457.

Notes

The authors declare no competing financial interest.

ACKNOWLEDGMENTS

For financial support of this work, we acknowledge the Los Alamos National Laboratory LDRD Program and G. T. Seaborg Institute (Fellowship to H.H.).

REFERENCES

- (1) He, H.; Qin, Z.; Shoesmith, D. W. Characterizing the Relationship between Hyperstoichiometry, Defect Structure and Local Corrosion Kinetics of Uranium Dioxide. *Electrochim. Acta* **2010**, *56*, 53–60.
- (2) He, H.; Shoesmith, D. W. Raman Spectroscopic Studies of Defect Structures and Phase Transition in Hyper-stoichiometric UO_{2+x} . *Phys. Chem. Chem. Phys.* **2010**, *12*, 8108–8117.
- (3) He, H.; Ding, Z.; Shoesmith, D. W. The Determination of Electrochemical Reactivity and Sustainability on Individual Hyper-Stoichiometric UO_{2+x} Grains by Raman Microspectroscopy and Scanning Electrochemical Microscopy. *Electrochem. Commun.* **2009**, *11*, 1724–1727.
- (4) Allen, G. C.; Holmes, N. R. A Mechanism for the UO_2 to α - U_3O_8 Phase Transformation. *J. Nucl. Mater.* **1995**, *223*, 231–237.
- (5) Allen, G. C.; Tempest, P. A. Ordered Defects in the Oxides of Uranium. *Proc. R. Soc. London, Ser. A* **1986**, *406*, 325–344.
- (6) Fujiwara, H. *Spectroscopic Ellipsometry Principles and Applications*; John Wiley & Sons: New York, 2007.
- (7) Aspnes, D. E. The Accurate Determination of Optical Properties by Ellipsometry. In *Handbook of Optical Constants of Solids*; Edward, D. P., Ed.; Academic Press: Burlington, MA, 1997; Chapter 5, pp 89–112.
- (8) Azzam, R. M. A.; Bashara, N. M. *Ellipsometry and Polarized Light*; North-Holland: Amsterdam, The Netherlands, 1987.
- (9) Azzam, R. M. A. *Selected Papers on Ellipsometry*; SPIE Optical Engineering Press: Bellingham, WA, 1991.
- (10) Dudarev, S. L.; Manh, D. N.; Sutton, A. P. Effect of Mott–Hubbard Correlations on the Electronic Structure and Structural Stability of Uranium Dioxide. *Philos. Mag. B* **1997**, *75*, 613–628.
- (11) Liechtenstein, A. I.; Anisimov, V. I.; Zaanen, J. Density-Functional Theory and Strong-Interactions — Orbital Ordering in Mott–Hubbard Insulators. *Phys. Rev. B* **1995**, *52*, 5467–5470.
- (12) Prodan, I. D.; Scuseria, G. E.; Martin, R. L. Assessment of Metageneralized Gradient Approximation and Screened Coulomb Hybrid Density Functionals on Bulk Actinide Oxides. *Phys. Rev. B* **2006**, *73*, 045104.
- (13) Roy, L. E.; Durakiewicz, T.; Martin, R. L.; Peralta, J. E.; Scuseria, G. E.; Olson, C. G.; Joyce, J. J.; Guziewicz, E. Dispersion in the Mott Insulator UO_2 : A Comparison of Photoemission Spectroscopy and Screened Hybrid Density Functional Theory. *J. Comput. Chem.* **2008**, *29*, 2288–2294.
- (14) Petit, L.; Svane, A.; Szotek, Z.; Temmerman, W. M.; Stocks, G. M. Electronic Structure and Ioncity of Actinide Oxides from First Principles. *Phys. Rev. B* **2010**, *81*, 045108.
- (15) Nam, H. V.; Hieu, V. L.; Thi, M. C.; Viet, V. P.; Hung, M. L.; Duc, N.-M. Anatase Rutile Phase Transformation of Titanium Dioxide Bulk Material: A DFT + *U* Approach. *J. Phys.: Condens. Matter* **2012**, *24*, 405501.
- (16) Meredig, B.; Thompson, A.; Hansen, H. A.; Wolverton, C.; van de Walle, A. Method for Locating Low-Energy Solutions within DFT +*U*. *Phys. Rev. B* **2010**, *82*, 195128.
- (17) Kudin, K. N.; Scuseria, G. E.; Martin, R. L. Hybrid Density-Functional Theory and the Insulating Gap of UO_2 . *Phys. Rev. Lett.* **2002**, *89*, 266402.

- (18) Yun, Y.; Rusz, J.; Suzuki, M. T.; Oppeneer, P. M. First-Principles Investigation of Higher Oxides of Uranium and Neptunium: U_3O_8 and Np_2O_5 . *Phys. Rev. B* **2011**, *83*, 075109.
- (19) Heyd, J.; Scuseria, G. E.; Ernzerhof, M. Hybrid Functionals Based on a Screened Coulomb Potential. *J. Chem. Phys.* **2003**, *118*, 8207–8215.
- (20) Jellison, J. G. E.; Modine, F. A. Parameterization of the Optical Functions of Amorphous Materials in the Interband Region. *Appl. Phys. Lett.* **1996**, *69*, 371–373.
- (21) Kresse, G.; Furthmüller, J. Efficiency of Ab-Initio Total Energy Calculations for Metals and Semiconductors Using a Plane-Wave Basis Set. *Comput. Mater. Sci.* **1996**, *6*, 15–50.
- (22) Kresse, G.; Furthmüller, J. Efficient Iterative Schemes for Ab Initio Total-Energy Calculations Using a Plane-Wave Basis Set. *Phys. Rev. B* **1996**, *54*, 11169–11186.
- (23) Kresse, G.; Hafner, J. Ab-Initio Molecular-Dynamics for Open-Shell Transition-Metals. *Phys. Rev. B* **1993**, *48*, 13115–13118.
- (24) Dudarev, S. L.; Manth, D. N.; Sutton, A. P. Effect of Mott–Hubbard Correlations on the Electronic Structure and Structural Stability of Uranium Dioxide. *Philos. Mag. B* **1997**, *75*, 613–628.
- (25) Liao, P. L.; Carter, E. A. Ab Initio DFT+U Predictions of Tensile Properties of Iron Oxides. *J. Mater. Chem.* **2010**, *20*, 6703–6719.
- (26) Poulesquen, A.; Desgranges, L.; Ferry, C. An Improved Model to Evaluate the Oxidation Kinetics of Uranium Dioxide during Dry Storage. *J. Nucl. Mater.* **2007**, *362*, 402–410.
- (27) Wen, X.-D.; Martin, R. L.; Scuseria, G. E.; Rudin, S. P.; Batista, E. R.; Burrell, A. K. Screened Hybrid and DFT + U Studies of the Structural, Electronic, and Optical Properties of U_3O_8 . *J. Phys.: Condens. Matter* **2013**, *25*, 025501.
- (28) Prodan, I.; Scuseria, G.; Martin, R. Covalency in the Actinide Dioxides: Systematic Study of the Electronic Properties Using Screened Hybrid Density Functional theory. *Phys. Rev. B* **2007**, *76*, 033101.
- (29) Wen, X.-D.; Martin, R. L.; Henderson, T. M.; Scuseria, G. E. Density Functional Theory Studies of the Electronic Structure of Solid State Actinide Oxides. *Chem. Rev.* **2012**, *113*, 1063–1096.
- (30) Perdew, J. P.; Chevary, J. A.; Vosko, S. H.; Jackson, K. A.; Pederson, M. R.; Singh, D. J.; Fiorelli, C. Atoms, Molecules, Solids, and Surfaces: Applications of the Generalized Gradient Approximation for Exchange and Correlation. *Phys. Rev. B* **1992**, *46*, 6671–6687.
- (31) Andersson, D. A.; Baldinozzi, G.; Desgranges, L.; Conradson, D. R.; Conradson, S. D. Density Functional Theory Calculations of UO_2 Oxidation: Evolution of UO_{2+x} , U_4O_{9-y} , U_3O_7 and U_3O_8 . *Inorg. Chem.* **2013**, *52*, 2769–2778.
- (32) Loopstra, B. O. On the Crystal Structure of $\alpha\text{-U}_3\text{O}_8$. *J. Inorg. Nucl. Chem.* **1977**, *39*, 1713–1714.
- (33) Blöchl, P. E.; Jepsen, O.; Andersen, O. K. Improved Tetrahedron Method for Brillouin-Zone Integrations. *Phys. Rev. B* **1994**, *49*, 16223–16233.
- (34) Andersson, D. A.; Uberuaga, B. P.; Nerikar, P. V.; Unal, C.; Stanek, C. R. U and Xe Transport in UO_{2+x} : Density Functional Theory Calculations. *Phys. Rev. B* **2011**, *84*, 054105.
- (35) Andersson, D. A.; Espinosa-Faller, F. J.; Uberuaga, B. P.; Conradson, S. D. Stability and Migration of Large Oxygen Clusters in UO_{2+x} : Density Functional Theory Calculations. *J. Chem. Phys.* **2012**, *136*, 234702.
- (36) Loopstra, B. O.; Cordfunke, E. H. P. On the Structure of $\alpha\text{-UO}_3$. *Recl. Trav. Chim. Pays-Bas* **1966**, *85*, 135–142.
- (37) Loopstra, B. O.; Taylor, J. C.; Waugh, A. B. Neutron Powder Profile Studies of the Gamma Uranium Trioxide Phases. *J. Solid State Chem.* **1977**, *20*, 9–19.
- (38) Weller, M. T.; Dickens, P. G.; Penny, D. J. The Structure of $\delta\text{-UO}_3$. *Polyhedron* **1988**, *7*, 243–244.
- (39) ICSD - Inorganic Crystal Structure Database. <http://www.fiz-karlsruhe.com/icsd.html> (2013).
- (40) Di, M.; Bersch, E.; Diebold, A. C.; Consiglio, S.; Clark, R. D.; Leusink, G. J.; Kaack, T. Comparison of Methods to Determine Band Gaps of Ultrathin HfO_2 Films Using Spectroscopic Ellipsometry. *J. Vac. Sci. Technol., A* **2011**, *29*, 041001/1–041001/8.
- (41) Davis, E. A.; Mott, N. F. Conduction in Non-Crystalline Systems V. Conductivity, Optical Absorption and Photoconductivity in Amorphous Semiconductors. *Philos. Mag.* **1970**, *22*, 0903–0922.
- (42) Urbach, F. The Long-Wavelength Edge of Photographic Sensitivity and of the Electronic Absorption of Solids. *Phys. Rev.* **1953**, *92*, 1324–1324.
- (43) Collins, R. W.; Vadam, K. Optical Properties of Solids. In *Digital Encyclopedia of Applied Physics*; WILEY-VCH Verlag GmbH & Co KGaA: New York, 2003.
- (44) Ferlauto, A. S.; Ferreira, G. M.; Pearce, J. M.; Wronski, C. R.; Collins, R. W.; Deng, X.; Ganguly, G. Analytical Model for the Optical Functions of Amorphous Semiconductors from the near-Infrared to Ultraviolet: Applications in Thin Film Photovoltaics. *J. Appl. Phys.* **2002**, *92*, 2424–2436.
- (45) Lee, B.-S.; Abelson, J. R.; Bishop, S. G.; Kang, D.-H.; Cheong, B.-k.; Kim, K.-B. Investigation of the Optical and Electronic Properties of $\text{Ge}_2\text{Sb}_2\text{Te}_5$ Phase Change Material in Its Amorphous, Cubic, And Hexagonal Phases. *J. Appl. Phys.* **2005**, *97*, 093509.
- (46) Cody, G. D.; Brooks, B. G.; Abeles, B. Optical Absorption above the Optical Gap of Amorphous Silicon Hydride. *Sol. Energy Mater.* **1982**, *8*, 231–240.
- (47) Idriss, H. Surface Reactions of Uranium Oxide Powder, Thin Films and Single Crystals. *Surf. Sci. Rep.* **2010**, *65*, 67–109.
- (48) He, H.; Wang, P.; Allred, D. D.; Majewski, J.; Wilkerson, M. P.; Rector, K. D. Characterization of Chemical Speciation in Ultra Thin Uranium Oxide Layered Films. *Anal. Chem.* **2012**, *84*, 10380–10387.
- (49) Greaves, C.; Fender, B. E. F. The Structure of $\alpha\text{-UO}_3$ by Neutron and Electron Diffraction. *Acta Crystallogr., Sect. B* **1972**, *28*, 3609–3614.
- (50) Nguyen, N. V.; Davydov, A. V.; Chandler-Horowitz, D.; Frank, M. M. Sub-Bandgap Defect States in Polycrystalline Hafnium Oxide and Their Suppression by Admixture of Silicon. *Appl. Phys. Lett.* **2005**, *87*, 192903/1–192903/3.
- (51) Bersch, E.; Di, M.; Consiglio, S.; Clark, R. D.; Leusink, G. J.; Diebold, A. C. Complete Band Offset Characterization of the $\text{HfO}_2/\text{SiO}_2/\text{Si}$ Stack Using Charge Corrected X-ray Photoelectron Spectroscopy. *J. Appl. Phys.* **2010**, *107*, 043702/1–043702/13.
- (52) Eriksen, T. E.; Jonsson, M.; Merino, J. Modelling of Time Resolved and Long Contact Time Dissolution Studies of Spent Nuclear Fuel in 10 mM Carbonate Solution — A Comparison between Two Different Models and Experimental Data. *J. Nucl. Mater.* **2008**, *375*, 331–339.
- (53) Ryzhkov, M. V.; Kupryazhkin, A. Y. First-Principles Study of Electronic Structure and Insulating Properties of Uranium and Plutonium Dioxides. *J. Nucl. Mater.* **2009**, *384*, 226–230.
- (54) Fillard, C.; Berthet, J. C.; Conradson, S. D.; Guilbaud, P.; Guillaumont, D.; Hennig, C.; Moisy, P.; Roques, J.; Simoni, E.; Shuh, D. K.; Tyliczszak, T.; Castro-Rodriguez, I.; Den Auwer, C. Combining Theoretical Chemistry and XANES Multi-Edge Experiments to Probe Actinide Valence States. *C. R. Chim.* **2007**, *10*, 859–871.
- (55) Govers, K.; Lemehov, S.; Hou, M.; Verwerft, M. Molecular Dynamics Simulation of Helium and Oxygen Diffusion in UO_{2+x} . *J. Nucl. Mater.* **2009**, *395*, 131–139.
- (56) Atta-Fynn, R.; Ray, A. K. Probing the 5f Electrons in Am-I by Hybrid Density Functional Theory. *Chem. Phys. Lett.* **2009**, *482*, 223–227.
- (57) Schoenes, J. Electronic Transitions, Crystal Field Effects and Phonons in UO_2 . *Phys. Rep.* **1980**, *63*, 301–336.
- (58) Schoenes, J. Optical Properties and Electronic Structure of UO_2 . *J. Appl. Phys.* **1978**, *49*, 1463–1465.
- (59) Schoenes, J. Recent Spectroscopic Studies of UO_2 . *J. Chem. Soc., Faraday Trans. 2* **1987**, *83*, 1205–1213.
- (60) Andersson, D. A.; Lezama, J.; Uberuaga, B. P.; Deo, C.; Conradson, S. D. Cooperativity among Defect Sites in AO_{2+x} and A_4O_9 ($\text{A} = \text{U}, \text{Np}, \text{Pu}$): Density Functional Calculations. *Phys. Rev. B* **2009**, *79*, 024110.

- (61) Dorado, B.; Amadon, B.; Freyss, M.; Bertolus, M. DFT+U Calculations of the Ground State and Metastable States of Uranium Dioxide. *Phys. Rev. B* **2009**, *79*, 235125.
- (62) Wen, X.-D.; Martin, R. L.; Roy, L. E.; Scuseria, G. E.; Rudin, S. P.; Batista, E. R.; McCleskey, T. M.; Scott, B. L.; Bauer, E.; Joyce, J. J.; Durakiewicz, T. Effect of Spin–Orbit Coupling on the Actinide Dioxides AnO_2 (An = Th, Pa, U, Np, Pu, and Am): A Screened Hybrid Density Functional Study. *J. Chem. Phys.* **2012**, *137*, 154707/1–154707/6.
- (63) Baer, Y.; Lang, J. K. High-Energy Spectroscopic Study of the Occupied and Unoccupied *Sf* and Valence States in Th and U Metals. *Phys. Rev. B* **1980**, *21*, 2060.
- (64) Barrett, N. T.; Greaves, G. N.; Willis, B. T. M.; Antonini, G. M.; Thornley, F. R. Anharmonic Vibrations in UO_2 As Determined by EXAFS. *J. Phys. C: Solid State Phys.* **1988**, *21*, L791–L796.
- (65) Andresen, A. The Structure of U_3O_8 Determined by Neutron Diffraction. *Acta Crystallogr.* **1958**, *11*, 612–614.
- (66) Sato, R.; Doi, H.; Ishii, B.; Uchikoshi, H. Reduction of U_3O_8 to U_3O_{8-x} in Mode of Crystallographic Out-of-Step. *Acta Crystallogr.* **1961**, *14*, 763–771.
- (67) Loopstra, B. Neutron Diffraction Investigation of U_3O_8 . *Acta Crystallogr.* **1964**, *17*, 651–654.
- (68) Singh, N.; Karkhanavala, M. D. Studies on the Electrical Properties of Uranium Oxides II. Non-stoichiometric U_3O_8 . *Phys. Status Solidi(B)* **1966**, *17*, 501–508.
- (69) Allen, G. C.; Holmes, N. R. Surface Characterisation of α -, β -, γ -, and δ - UO_3 Using X-ray Photoelectron Spectroscopy. *J. Chem. Soc., Dalton Trans.* **1987**, 3009–3015.
- (70) Moine, P.; Naudon, A.; Kim, J. J.; Marshall, A. F.; Stevenson, D. A. Characterization of Ni–Ti Alloys Synthesized by Vapor Quenching. *J. Phys. Colloq.* **1985**, *46*, 223–227.
- (71) Bechhoefer, J.; Löwen, H.; Tuckerman, L. S. Dynamical Mechanism for the Formation of Metastable Phases. *Phys. Rev. Lett.* **1991**, *67*, 1266–1269.